



Mechanism and micro-kinetics of direct N₂O decomposition over BaFeAl₁₁O₁₉ hexaaluminate and comparison with Fe-MFI zeolites

Evgenii V. Kondratenko^{a,*}, Vita A. Kondratenko^a, Marta Santiago^b, Javier Pérez-Ramírez^b

^a Leibniz-Institut für Katalyse e. V. an der Universität Rostock, Albert-Einstein-Strasse 29a, D-18059 Rostock, Germany

^b Institute for Chemical and Bioengineering, Department of Chemistry and Applied Biosciences, ETH Zürich, HCI E 125, Wolfgang-Pauli-Strasse 10, CH-8093 Zurich, Switzerland

ARTICLE INFO

Article history:

Received 7 April 2010

Received in revised form 26 May 2010

Accepted 28 May 2010

Available online 17 June 2010

Keywords:

N₂O decomposition

Iron hexaaluminate

Fe-ZSM-5

Oxygen formation

Mechanism

Micro-kinetics

TAP reactor

ABSTRACT

Mechanistic and kinetic aspects of direct N₂O decomposition over BaFeAl₁₁O₁₉ hexaaluminate were investigated in the Temporal Analysis of Products (TAP) reactor and compared with those previously determined for Fe-MFI zeolites. The catalysts were chosen due to their de-N₂O operation in significantly different temperature regimes. Several micro-kinetic models were evaluated for describing the transient responses of N₂O, N₂, and O₂ obtained in N₂O pulse experiments at 823–973 K. Thorough discrimination between these models enabled us to conclude that the preferred models of N₂O decomposition over BaFeAl₁₁O₁₉ and Fe-MFI zeolites differ in the reaction pathways leading to O₂ and N₂. Gas-phase N₂ and O₂ are simultaneously formed over BaFeAl₁₁O₁₉ upon interaction of gas-phase N₂O with a bi-atomic surface oxygen (*–O₂) species. Contrarily, the formation of O₂ over Fe-MFI occurs via a sequence of three elementary heterogeneous steps and limits the overall rate of N₂O decomposition. Despite the easy O₂ formation, BaFeAl₁₁O₁₉ is less active for N₂O decomposition below 973 K than the Fe-MFI zeolites due to the low coverage by *–O₂. According to our quantitative micro-kinetic analysis, this species is formed when gas-phase N₂O reacts with a mono-atomic oxygen (*–O) species. This reaction pathway is strongly influenced by the degree of isolation of iron species. The higher the degree of iron isolation in the catalyst, the lower the de-N₂O activity.

© 2010 Elsevier B.V. All rights reserved.

1. Introduction

In recent years, a number of bulk and supported mixed-metal oxides as well as metal-loaded zeolites have been implemented for catalytic N₂O removal from the off-gases of adipic and nitric acid production plants, the main sources of this harmful gas in the chemical industry [1–3]. Iron-containing zeolites (particularly Fe-ZSM-5) are probably the most extensively studied catalytic materials because they reveal outstanding activity and stability for N₂O removal in the presence of typical off-gas components (O₂, NO_x, and H₂O) [4–6]. These catalytic features stimulated many studies for elucidating the nature of iron species active in N₂O decomposition [7–13] as well as for deriving reaction mechanisms and kinetics [11,14–25].

Several reaction schemes have been suggested for direct N₂O decomposition over Fe-MFI zeolites [1,14,25]. They differ in the pathways leading to N₂ and O₂. N₂O decomposition is initiated by the interaction of gas-phase N₂O with an active iron site resulting in the gas-phase N₂ and adsorbed oxygen species (*–O). The formation of O₂ was originally explained either by (i) recombination

of two *–O species [14] or by (ii) direct reaction of gas-phase N₂O with *–O [15]. Recent micro-kinetic schemes derived from Density Functional Theory (DFT) simulations [20–22] and transient studies in the Temporal Analysis of Products (TAP) reactor [23–25] revealed that the mechanism of O₂ formation comprises a more complex sequence of elementary reaction steps: (i) N₂O reacts with an active oxygen species (*–O) yielding an intermediate bi-atomic oxygen species (O–*–O), (ii) the latter species reorganizes into another bi-atomic form (*–O₂), and (iii) *–O₂ desorbs as gas-phase oxygen regenerating the active site. TAP studies [23–25] proved that the reaction mechanism was neither influenced by the nature of the iron species in the zeolite (isolated versus oligomeric), the composition of the MFI framework (ZSM-5 versus silicalite), nor by the method of iron incorporation (hydrothermal synthesis followed by steam activation versus liquid-ion exchange). Moreover, the TAP-derived micro-kinetic model was extrapolated to a wide range of N₂O partial pressures (0.01–15 kPa) and temperatures (473–873 K). As a result, differences in the steady-state de-N₂O performance of zeolite samples with different iron speciation could be qualitatively predicted.

Fe-MFI zeolites find industrial application for N₂O decomposition in the tail gases of nitric acid plants [2], operating optimally in the temperature range of 673–773 K. Process-gas N₂O decomposition in the ammonia burner is also industrially applied as a

* Corresponding author.

E-mail address: evgenii.kondratenko@catalysis.de (E.V. Kondratenko).

cost-effective, robust, and versatile technology for N_2O abatement in this source. In this case, suitable catalysts are located directly under Pt-Rh gauzes and typically operate above 1073 K. They must possess high chemical stability to withstand the demanding conditions inside the ammonia burner (high-temperature, wet oxidizing atmosphere). LaCoO_3 perovskite and CeO_2 -supported Co_2AlO_4 have been successfully implemented in large scale [2], although other families of mixed oxides proved to be active and stable in laboratory tests [26–33]. However, very little studies have addressed the mechanism of N_2O decomposition over catalysts operating at high temperatures (>873 K). Exceptionally, Ivanov et al. [34] studied the direct N_2O decomposition using the Steady-State Isotopic Transient Kinetic Analysis (SSITKA) and highlighted the importance of oxygen mobility for the de- N_2O activity over La-Sr-Mn perovskite-type oxides.

To the best of our knowledge, no studies have established mechanistic analogies and differences in direct N_2O decomposition over catalysts operating in high (>873 K) and low-temperature (<723 K) regimes. Herein, we have carried out a detailed mechanistic and micro-kinetic analysis of N_2O decomposition over $\text{BaFeAl}_{11}\text{O}_{19}$ hexaaluminate using the TAP reactor and the mathematical approach applied earlier for the study of N_2O decomposition over iron-containing zeolites [23–25]. The aim of this analysis was to identify mechanistic aspects governing the distinct de- N_2O performance of $\text{BaFeAl}_{11}\text{O}_{19}$ and Fe-MFI catalysts. This particular hexaaluminate was chosen due to its remarkable process-gas de- N_2O performance under simulated conditions of nitric acid plants [28,29].

2. Experimental

2.1. Catalyst

$\text{BaFeAl}_{11}\text{O}_{19}$ was prepared by coprecipitation of the corresponding precursors using the in-line dispersion precipitation (ILDp) method [35] followed by high-temperature calcination. An aqueous solution of the metal nitrates (0.1 M Ba, 0.1 M Fe, and 1.1 M Al) and a 2 M aqueous solution of $(\text{NH}_4)_2\text{CO}_3$ were pumped into a 6 ml reactor attached to a high-shear homogenizer rotating at 13,500 rpm. The pH of the slurry was measured and controlled by an in-line probe directly at the outlet of the precipitation chamber. Coprecipitation was carried out at constant pH 8 with an average residence time of 18 s. The slurry was aged at 333 K for 3 h, filtered, washed thoroughly, and dried at 353 K for 12 h. The resulting solid was calcined in static air at 1473 K for 10 h using a heating rate of 5 K min^{-1} . Characterization of the catalyst by inductively coupled plasma optical emission spectroscopy (ICP-OES), X-ray diffraction, and N_2 adsorption was presented elsewhere [29]. The molar metal ratios in the mixed oxide were very close to the nominal values. The sample showed hexaaluminate ($\text{BaFeAl}_{11}\text{O}_{19}$, JCPDS 26-135) as the only crystalline phase and possessed a total surface area (S_{BET}) of $12 \text{ m}^2 \text{ g}^{-1}$.

2.2. Continuous flow catalytic tests at ambient pressure

Steady-state N_2O decomposition tests were carried out in a Micro Activity Reference setup (PID Eng&Tech) using a quartz micro-reactor (9 mm i.d.). The catalyst (100 mg, sieve fraction 125–300 μm) was loaded between two layers of quartz wool and rested over a porous frit. The sample was pre-treated in He at 673 K for 1 h and cooled down to the initial reaction temperature (473 K). Then, the feed mixture (1.5 mbar N_2O in He) was introduced into the reactor with a space velocity of $60,000 \text{ ml g}^{-1} \text{ h}^{-1}$. The temperature was increased at intervals of 50 K up to 973 K, using a heating rate of 5 K min^{-1} and keeping an isothermal period

of 30 min at each set point. In this period, constant conversion levels were obtained. Reactant and product gases were analyzed by on-line gas chromatography (Agilent 6890N).

2.3. Transient experiments in vacuum

Direct N_2O decomposition was investigated in the Temporal Analysis of Products (TAP-2) reactor, a transient pulse technique operating in vacuum with sub-millisecond time resolution [36,37]. The $\text{BaFeAl}_{11}\text{O}_{19}$ sample (20 mg, sieve fraction of 250–350 μm) was packed within the isothermal zone of the quartz micro-reactor (40 mm length and 6 mm i.d.) between two layers of quartz particles of the same sieve fraction. The catalyst was pre-treated in flowing O_2 (30 ml STP min^{-1}) at 1023 K and atmospheric pressure for 1 h, followed by exposure to vacuum (10^{-5} Pa), and cooling down to 823 K. Thereafter, a mixture of $\text{N}_2\text{O}:\text{Ne} = 1:1$ was pulsed in the temperature range of 823–973 K with 50 K intervals, starting from 823 K. The ramping from one temperature to the next one was performed in vacuum. After each set point was reached, the catalyst was pre-treated using large N_2O pulses (ca. 10^{16} molecules) in order to recover surface oxygen species, which could have partially desorbed under vacuum conditions. Thereafter, low-sized N_2O pulses (5×10^{14} – 1×10^{15} molecules) were injected into the micro-reactor. These experiments were used for micro-kinetic analysis of N_2O decomposition. Under these conditions, Knudsen diffusion describes the gas transport inside the reactor and the transient responses are a function of gas–solid interactions, i.e. they are not influenced by molecular collisions in the gas-phase.

A quadrupole mass spectrometer (HAL RC 301 Hiden Analytical) was used for quantitative analysis of reactants and reaction products. The transient responses at the reactor outlet were monitored at the following atomic mass units (AMUs): 44 (N_2O), 32 (O_2), 30 (N_2O , NO), 28 (N_2 , N_2O), and 20 (Ne). In the experiments, 10 pulses for each AMU were averaged in order to improve the signal-to-noise ratio. The concentrations of feed components and reaction products were determined from the corresponding AMUs using standard fragmentation patterns and sensitivity factors according to [25].

2.4. Kinetic evaluation of transient experiments

The parameter estimation procedure used here was reported elsewhere [38,39]. Briefly, it is based on a numerical solution of partial differential equations (PDEs) describing diffusion, adsorption, desorption, and reaction in the TAP micro-reactor. PDEs were transformed into coupled ordinary differential equations (ODEs) by spatial approximation and then integrated numerically using the PDEONE routine [40]. Parameters (rate and diffusion coefficients) were determined using first a genetic algorithm to find good starting values [41] and then the Nelder–Mead simplex algorithm [42]. The TAP micro-reactor was described as a one-dimensional pseudo-homogeneous system divided into three zones, which are represented by the catalyst and the two layers of inert material, where the catalyst was sandwiched.

The transport of gaseous compounds was described by Knudsen diffusion along the reactor axis. Experimental transient responses of N_2O , O_2 , and N_2 were simultaneously used for the fitting procedure. The N_2 response was corrected with respect to the contribution of the N_2O response according to the fragmentation patterns determined upon pulsing of $\text{N}_2\text{O}:\text{Ne} = 1:1$ over SiO_2 particles (inert bed). Each response was described by representative points as reported elsewhere [39]. The goodness of the fit was determined by an objective function defined as the sum of squares of the shortest deviations between the respective pairs of points of the experimental and simulated transient responses [39]. For the best kinetic model, we have performed both sensitivity and correlation

Table 1
Micro-kinetic models evaluated in this work.

| Model | Elementary reaction steps | |
|-------|--|-------|
| 1 | $\text{N}_2\text{O} + * \rightarrow \text{N}_2 + *-\text{O}$ | (1.1) |
| | $*-\text{O} + *-\text{O} \rightarrow \text{O}_2 + 2*$ | (1.2) |
| 2 | $\text{N}_2\text{O} + * \rightarrow \text{N}_2 + *-\text{O}$ | (2.1) |
| | $\text{N}_2\text{O} + *-\text{O} \rightarrow \text{N}_2 + \text{O}_2 + *$ | (2.2) |
| 3 | $\text{N}_2\text{O} + * \rightarrow \text{N}_2 + *-\text{O}$ | (3.1) |
| | $*-\text{O} + *-\text{O} \rightarrow *-\text{O}_2 + *$ | (3.2) |
| | $*-\text{O}_2 \rightarrow \text{O}_2 + *$ | (3.3) |
| 4 | $\text{N}_2\text{O} + * \rightarrow \text{N}_2 + *-\text{O}$ | (4.1) |
| | $\text{N}_2\text{O} + *-\text{O} \rightarrow \text{N}_2 + *-\text{O}_2$ | (4.2) |
| | $\text{N}_2\text{O} + *-\text{O}_2 \rightarrow \text{N}_2 + \text{O}-*-\text{O}_2$ | (4.3) |
| | $\text{O}-*-\text{O}_2 \rightarrow \text{O}_2 + *-\text{O}$ | (4.4) |
| | $*-\text{O}_2 \rightarrow \text{O}_2 + *$ | (4.5) |
| 5 | $\text{N}_2\text{O} + * \rightarrow \text{N}_2 + *-\text{O}$ | (5.1) |
| | $\text{N}_2\text{O} + *-\text{O} \rightarrow \text{N}_2 + *-\text{O}_2$ | (5.2) |
| | $\text{N}_2\text{O} + *-\text{O}_2 \rightarrow \text{N}_2 + *-\text{O} + \text{O}_2$ | (5.3) |
| | $*-\text{O}_2 \rightarrow \text{O}_2 + *$ | (5.4) |
| | $\text{O}_2 + * \rightarrow *-\text{O}_2$ | (5.5) |
| 6 | $\text{N}_2\text{O} + * \rightarrow \text{N}_2 + *-\text{O}$ | (6.1) |
| | $\text{N}_2\text{O} + *-\text{O} \rightarrow \text{N}_2 + *-\text{O}_2$ | (6.2) |
| | $*-\text{O}_2 \rightarrow \text{O}_2 + *$ | (6.3) |
| | $*-\text{O} + *-\text{O} \rightarrow 2* + \text{O}_2$ | (6.4) |
| 7 | $\text{N}_2\text{O} + * \rightarrow \text{N}_2 + *-\text{O}$ | (7.1) |
| | $\text{N}_2\text{O} + *-\text{O} \rightarrow \text{N}_2 + *-\text{O}_2$ | (7.2) |
| | $*-\text{O}_2 \rightarrow \text{O}_2 + *$ | (7.3) |
| | $*-\text{O} + *-\text{O} \rightarrow *-\text{O}_2 + *$ | (7.4) |
| | $*-\text{O}_2 + * \rightarrow *-\text{O} + *-\text{O}$ | (7.5) |
| 8 | $\text{N}_2\text{O} + * \rightarrow \text{N}_2 + *-\text{O}$ | (8.1) |
| | $\text{N}_2\text{O} + *-\text{O} \rightarrow \text{N}_2 + *-\text{O}_2$ | (8.2) |
| | $\text{N}_2\text{O} + *-\text{O}_2 \rightarrow \text{N}_2 + *-\text{O}_3$ | (8.3) |
| | $*-\text{O}_2 \rightarrow \text{O}_2 + *$ | (8.4) |
| | $*-\text{O}_3 \rightarrow *-\text{O} + \text{O}_2$ | (8.5) |
| 9 | $\text{N}_2\text{O} + * \rightarrow \text{N}_2 + *-\text{O}$ | (9.1) |
| | $\text{N}_2\text{O} + *-\text{O} \rightarrow \text{N}_2 + \text{O}-*-\text{O}$ | (9.2) |
| | $\text{O}-*-\text{O} \rightarrow *-\text{O}_2$ | (9.3) |
| | $*-\text{O}_2 \rightarrow \text{O}_2 + *$ | (9.4) |

analysis in order to validate the kinetic parameters. In the sensitivity analysis, each parameter was varied until the objective function changed by 10%.

The micro-kinetic models of direct N_2O decomposition evaluated in this work are listed in Table 1. Based on the results of the model discrimination at a reference temperature (T_{ref}) of 923 K, the best model was selected for simultaneous fitting of the transient responses at other temperatures. To avoid the correlation between activation energies and pre-exponential factors [43,44], activation energies for all elementary reaction steps were derived according to the equation:

$$k_{T_i} = k_{T_{\text{ref}}} \cdot \exp \left(-\frac{E_a}{R} \cdot \left(\frac{1}{T_i} - \frac{1}{T_{\text{ref}}} \right) \right)$$

where T_{ref} and $k_{T_{\text{ref}}}$ are the reference temperature and the rate coefficient at this temperature, respectively.

3. Results and discussion

3.1. N_2O decomposition under steady-state ambient pressure and vacuum transient conditions

Fig. 1 compares the N_2O conversion under vacuum transient and ambient pressure steady-state conditions. A higher de- N_2O activity in vacuum compared to the ambient pressure tests can be tentatively explained by the partial reduction of the catalyst surface, increasing the number of oxygen vacancies, which are potential active sites for N_2O decomposition. There are several studies high-

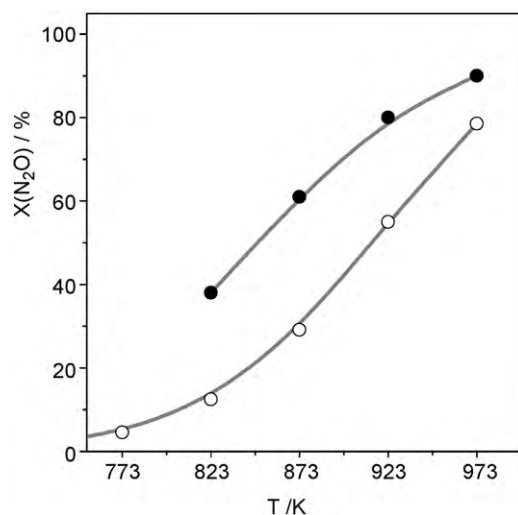


Fig. 1. N_2O conversion versus temperature over $\text{BaFeAl}_{11}\text{O}_{19}$ under (○) ambient pressure steady-state tests in a continuous flow reactor and (●) vacuum transient conditions in the TAP reactor.

lighting the importance of high-temperature catalyst treatment (in vacuum, inert atmosphere, steam, or hydrogen) for increasing the de- N_2O activity. Originally, Panov and co-workers [9] reported that such treatment of Fe-MFI zeolites results in the reduction of Fe^{3+} to Fe^{2+} , which forms the so-called α -sites. Berrier et al. [13] demonstrated that the concentration of active oxygen species formed upon N_2O decomposition over Fe-MFI zeolites increased when the temperature of catalyst pre-reduction in flowing H_2 raised from 673 to 873 K. Similar results were reported for Fe-FER and Fe-BEA, when the catalysts were treated in Ar at 723 and 923 K [45]. Centi et al. [46] observed an increase in the de- N_2O activity of Rh and Ni-containing catalysts after their reduction in an H_2 flow at 773 K. They suggested that the reduction of metal oxides to metals resulted in an increase in the initial de- N_2O activity.

Our further discussion focuses on the analysis and kinetic evaluation of transient N_2O decomposition experiments by Temporal Analysis of Products. Following our previous approach applied for metal-loaded zeolites [25], model-free mechanistic insights into N_2O decomposition over $\text{BaFeAl}_{11}\text{O}_{19}$ hexaaluminate were derived from the analysis of the order of appearance and the shapes of the height-normalized transient responses of N_2O , N_2 , and O_2 (Fig. 2).

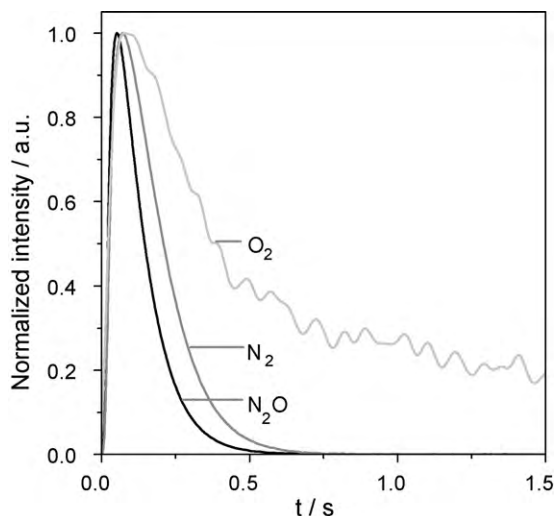


Fig. 2. Normalized transient responses of N_2O , N_2 , and O_2 upon N_2O pulsing over $\text{BaFeAl}_{11}\text{O}_{19}$ at 873 K ($\text{N}_2\text{O}:\text{Ne} = 1:1$, pulse size $\sim 10^{15}$ molecules).

For example, the times of the maximal concentration (t_{\max}) of N_2 (0.072 s) and O_2 (0.075 s) at 873 K are very close to each other but they are significantly higher than the t_{\max} value of N_2O (0.045 s). The similarity of the t_{\max} of N_2 and O_2 indicates that the reaction pathways leading to these products occur with similar rates. In contrast to the N_2 response, the O_2 response is characterized by a long tailing (slow decrease in the O_2 concentration with time). This tailing indicates that (i) the formed O_2 readsorbs over the catalyst and/or (ii) there are several elementary reaction pathways leading to gas-phase O_2 .

3.2. Micro-kinetic analysis

According to the theory of the TAP reactor [36,37], the shape and the order of appearance of the transient N_2O , N_2 , and O_2 responses contain information about the mechanism and kinetics of N_2O decomposition. This information can be extracted from kinetic evaluation of these responses. In the present study, different micro-kinetic models listed in Table 1 were used and discriminated for simultaneous fitting of the reactant and products responses according to [38,39]. The models are based on previous experimental or DFT (density functional theory) results of N_2O decomposition over Fe-MFI zeolites. It is beyond the scope of our modeling approach to take the structure of the active sites and the charge of oxygen species formed from N_2O into consideration. Since no experimental insights into reversible N_2O adsorption could be derived from the present study, the first step of N_2O decomposition in all the applied models was described by the decomposition of gas-phase N_2O over a free surface site (*). This reaction yields gas-phase N_2 and mono-atomic *-O species. Various subsequent reactions of this oxygen species, which could yield gas-phase O_2 , were considered in the models. The formation of gas-phase O_2 in models 1 and 6 is described by direct recombination of two mono-atomic *-O species as suggested in [14,47]. O_2 formation via decomposition of a surface bi-atomic oxygen precursor originated by recombination of two mono-atomic *-O species is considered in models 3 and 7 [17,48,49]. Model 2 assumes a direct reaction of gas-phase N_2O with *-O yielding gas-phase O_2 [15]. This reaction pathway was modified in models 4, 5, and 8 by taking into account that surface bi-atomic or tri-atomic oxygen species are formed upon interaction of gas-phase N_2O with mono-atomic *-O species or bi-atomic *-O₂ species, respectively, as suggested in [21,23,25]. Decomposition of surface *-O₂ species to gas-phase O_2 is considered in models 3, 5–9.

For model discrimination, the fitting procedure was repeated at least three times with each model. Since a solution might be not found within the first fitting in an n -dimensional parameters space, the second and third fitting avoids wrong discarding of a model. The reaction scheme in model 5 provided the best description of all transient responses in the temperature range investigated (Fig. 3). According to this model, a bi-atomic oxygen species is formed when N_2O decomposes over *-O. This species can be ascribed to a peroxo one and can be stabilized by the presence of barium in BaFeAl₁₁O₁₉. The formation of barium peroxide at high temperatures was proven experimentally in several studies [50–52]. The optimized values for kinetic parameters in model 5 are listed in Table 2. It should be noted that k^0 values determined for reaction pathways 1 and 2 relate to the apparent kinetic constants ($k_i \times C_{\text{total}}$), since our modeling approach does not enable to determine independently the intrinsic reaction constants and the total number of surface sites. The low activation energy of O_2 formation via step 4 in Table 2 may be due to facilitated O_2 desorption in high vacuum. The kinetic parameters of model 5 were additionally validated by sensitivity and correlations analysis (Section 2.4). The correlation coefficients between the individual parameters deviated significantly (at least by 10% for the kinetic constants for steps 2 and 3 in Table 2) from the boundary values of –1 and 1 characteristic for a straight cor-

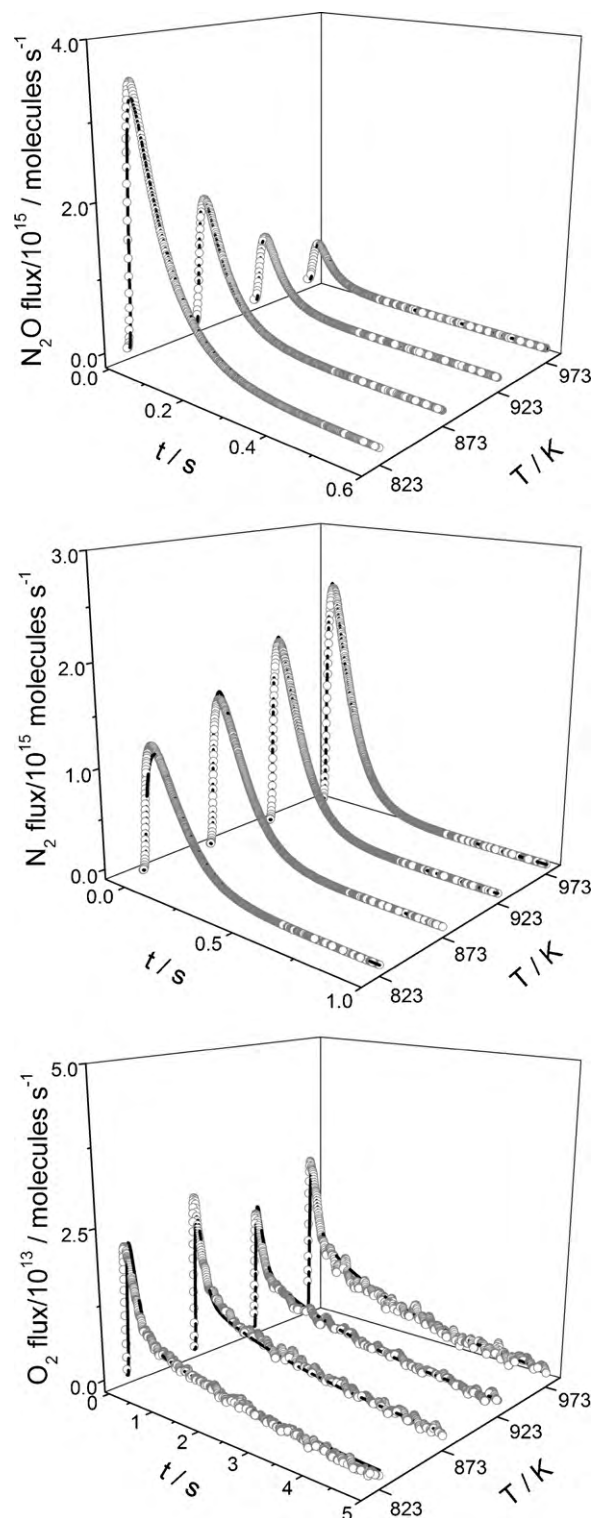


Fig. 3. Experimental (symbols) and calculated (lines) transient responses of N_2O , N_2 , and O_2 using model 5 in Table 1 for N_2O decomposition over BaFeAl₁₁O₁₉ at different temperatures.

relation. The accuracy of the kinetic parameters for steps 1–4 was higher than 8% as derived from the sensitivity analysis. The error for the kinetic parameter for step 5 was higher than 100%. This is probably because the low dependence of N_2O decomposition on the partial O_2 pressure experimentally determined in [28,29] cannot be properly derived from low-pressure single N_2O pulse experiments in the present study. This previous experimental anal-

Table 2

Best kinetic model and parameters of N₂O decomposition over BaFeAl₁₁O₁₉ derived from transient experiments in the TAP reactor^a.

| No | Elementary reaction steps | k^0 (s ⁻¹) | E_a (kJ mol ⁻¹) |
|----|---|--------------------------|-------------------------------|
| 1 | N ₂ O + * → *-O + N ₂ | 1.3×10^6 | 137 |
| 2 | N ₂ O + *-O → *-O ₂ + N ₂ | 4.9×10^2 | 97 |
| 3 | N ₂ O + *-O ₂ → *-O + N ₂ + O ₂ | 1.8×10^1 | 62 |
| 4 | *-O ₂ → O ₂ + * | 2.0×10^0 | 10 |
| 5 | O ₂ + * → *-O ₂ | 1.6×10^4 | 173 |

^a For steps 1–3, the pre-exponential factors are in Pa⁻¹ s⁻¹.

ysis reported only 40% decrease in the degree of N₂O conversion, when N₂O decomposition was investigated using a feed mixture with O₂/N₂O ratio = 7.

It is also important to stress that models 4, 7, and 8 contain the same number of parameters as model 5 but failed to correctly describe the N₂O, N₂, and O₂ transient responses. This fact supports that model 5 is suitable for N₂O decomposition from a mathematic point of view and physically also reflects the reaction mechanism over this catalyst. This model differs from that describing N₂O decomposition over Fe-MFI zeolites [23–25]. Section 3.4 discusses in detail these mechanistic differences with the aim to determine mechanistic origins of the distinctive de-N₂O activity of these catalysts.

In summary, the decomposition of N₂O over BaFeAl₁₁O₁₉ proceeds via interaction of gas-phase N₂O with free (*) Fe sites as well as with Fe sites occupied by mono (*-O) and bi-atomic (*-O₂) oxygen species originated from N₂O decomposition. All these iron sites were considered to be active for N₂O decomposition over Fe-MFI zeolites, too [20–25]. Gas-phase O₂ is formed via decomposition of the bi-atomic oxygen species (step 4 in Table 2) or their reaction with gas-phase N₂O (step 3 in Table 2). These reaction pathways were discussed for direct N₂O decomposition over Rh-ZSM-5 [25] and Fe-ZSM-5 [20–22], respectively. Since the activation energies of O₂ formation are lower than those of N₂ formation via steps 1 and 2 in Table 2 as well as O₂ and N₂ are simultaneously formed via step 3 in Table 2, it is put forward that the decomposition of N₂O over BaFeAl₁₁O₁₉ is not limited by O₂ desorption. This conclusion from micro-kinetic modeling is supported by experiments (Fig. 2); O₂ and N₂ appear at the reactor outlet after very similar times upon N₂O pulsing.

3.3. Model validation and analysis

As discussed above, model 5 correctly describes the experimental data of N₂O decomposition over BaFeAl₁₁O₁₉ under transient conditions. In order to validate this model, we calculated the rates of N₂O decomposition under steady-state conditions using kinetic parameters derived from the fitting of TAP responses (Table 2) and compared these rates with those of N₂O decomposition over Fe-MFI zeolites. For the latter catalysts, the micro-kinetic model and the respective parameters were taken from our previous works [23,25]. These studies proved that the TAP-derived kinetics of N₂O decomposition predicted correctly the steady-state performance. Similar to the iron-containing zeolite catalysts, the rate of N₂O decomposition over BaFeAl₁₁O₁₉ increases linearly with the partial N₂O pressure (first-order dependence). In contrast to previous results of N₂O decomposition over the same hexaaluminate under flow conditions at ambient pressure [28,29], our micro-kinetics predicts too low negative effect of O₂ on the rate of N₂O decomposition. A possible reason for this discrepancy was discussed in the preceding section.

The rates of N₂O decomposition were calculated in the temperature range of 673–973 K and partial N₂O pressure of 150 Pa. As shown in Fig. 4b, all the rates increase with temperature. It is also clearly seen that our calculations predict the lowest activity of

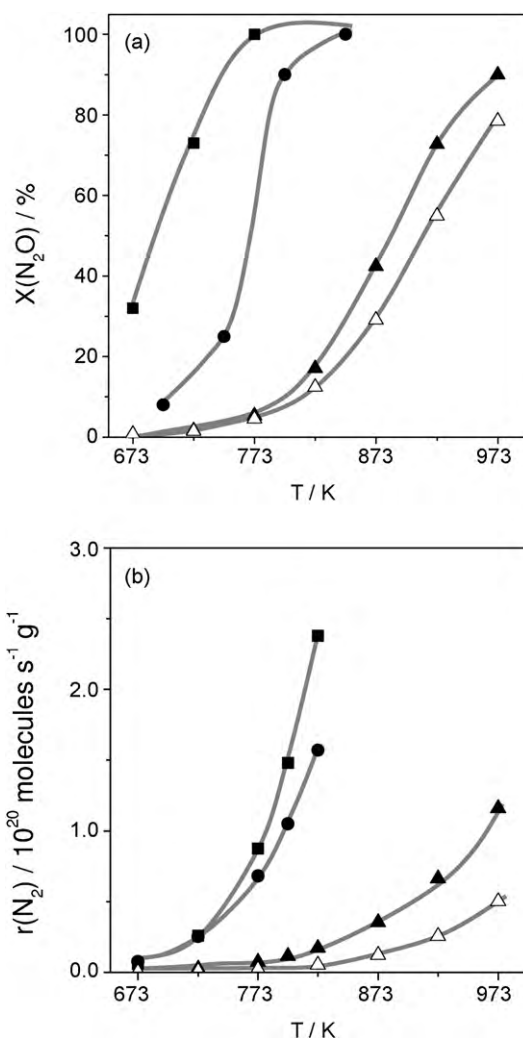


Fig. 4. De-N₂O performance of (Δ) BaFeAl₁₁O₁₉, (▲) Fe-silicalite(st), (●) Fe-ZSM-5(st), and (■) Fe-ZSM-5(lie) versus temperature: (a) N₂O conversion determined experimentally [10,28], and (b) rates of N₂ formation calculated with the kinetic parameters from Tables 2 and 3.

BaFeAl₁₁O₁₉ and the different activity of the Fe-MFI zeolites. A similar activity order is also valid for experimentally determined N₂O conversion over all these catalysts under steady-state conditions at partial N₂O pressure of 150 Pa (Fig. 4a).

In order to elucidate the contribution of empty sites (*) as well as *-O, and *-O₂ species to the overall rate of N₂O decomposition over BaFeAl₁₁O₁₉ under steady-state conditions, the surface coverage by these species at different temperatures and partial N₂O pressures were computed with the kinetic parameters in Table 2. Fig. 5 illustrates the coverage by these species during steady-state N₂O decomposition at 873, 973, and 1073 K. The partial N₂O pressure was in the range of 1–1000 Pa representing the profile of N₂O concentration along the catalyst bed used for N₂O decomposition in the nitric acid plants. Mono-atomic oxygen (*-O) is the dominant species in the whole range of partial N₂O pressures. Its coverage slightly decreases with an increase in temperature. The coverage by *-O₂ continuously increases with temperature and partial N₂O pressure, while the coverage by free active sites (*) decreases. The steady-state simulation predicts that the *-O and *-O₂ are major active species participating in the formation of N₂ from N₂O. Concerning the formation of gas-phase O₂, it is suggested that it is predominantly formed via the interaction of gas-phase N₂O and *-O₂ (step 3 in Table 2). Desorption of *-O₂ to gas-phase O₂ (step

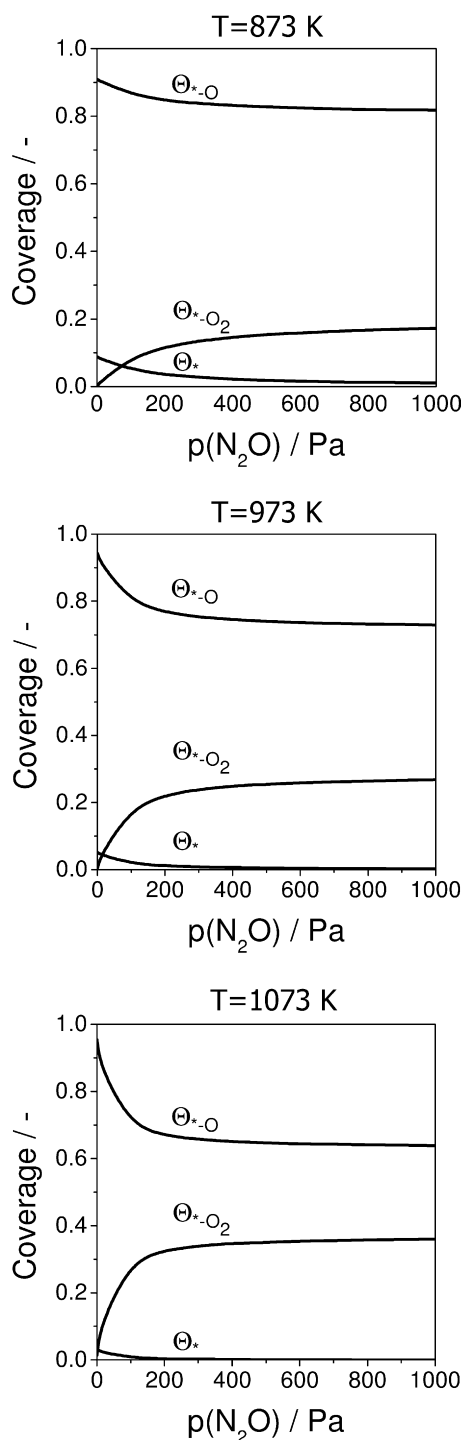


Fig. 5. Calculated steady-state coverage by surface species upon N_2O decomposition over $\text{BaFeAl}_{11}\text{O}_{19}$ at different temperatures for inlet partial N_2O pressures in the range of 1–1000 Pa. Kinetic parameters for the calculation were taken from Table 2.

4 in Table 2) plays a role at low partial N_2O pressures and temperatures. This is due to the fact that the O_2 formation via step 3 is influenced by the partial N_2O pressure and has significantly higher activation energy than O_2 formation via step 4.

In order to derive insights into the nature of active species during N_2O decomposition under vacuum transient conditions, we calculated temporal and spatial coverages by surface oxygen species during N_2O pulse experiments in the TAP reactor. In agreement with the steady-state experiments, mono-atomic oxygen (*O) is also the dominant species under transient conditions. At similar

partial N_2O pressures, the coverage by *O_2 is, however, higher in the TAP experiments than in ambient pressure steady-state conditions. Since these bi-atomic oxygen species disappear via reaction with gas-phase N_2O , this difference in the coverage can be due to a lower contribution of this reaction pathway to the overall N_2O decomposition at low partial N_2O partial pressures (peak pressure in the TAP experiments was below 5 Pa). This conclusion is supported by our calculations of the steady-state rates of N_2 formation over various active sites at different partial N_2O pressures. These rates over free (*) and mono-atomic oxygen species (*O) at 873 K are higher than that over *O_2 at pressures below 100 Pa. While the contribution of *O_2 to N_2O decomposition increases with temperature, that of free sites decreases.

3.4. Effect of FeO_x species and host matrix on the de- N_2O activity

Finally, we shall discuss the derived micro-kinetics for identifying mechanistic origins of the distinct de- N_2O activity of $\text{BaFeAl}_{11}\text{O}_{19}$ and Fe-MFI catalysts [23–25]. Along the manuscript, the zeolites are denoted as Fe-silicalite(st), Fe-ZSM-5(st), and Fe-ZSM-5(lie). They differ in the method of iron incorporation, i.e. liquid-ion exchange (lie), and hydrothermal synthesis followed by calcination and steam treatment(st). For all the catalysts investigated, the TAP-derived micro-kinetic schemes of N_2O decomposition predict that both free active sites (*) and sites occupied by mono-atomic oxygen species (*O) participate in N_2O decomposition. In addition, *O_2 species formed over $\text{BaFeAl}_{11}\text{O}_{19}$ via an interaction of *O with N_2O (step 3 in Table 2) are also active sites for N_2O decomposition. Gas-phase N_2O directly decomposes over all the above sites.

The calculated activation energies (E_a) of N_2O decomposition over free active sites (*) on $\text{BaFeAl}_{11}\text{O}_{19}$, Fe-silicalite(st), and Fe-ZSM-5(lie) are 137, 120, and 130 kJ mol^{-1} , respectively (Tables 2 and 3). Such close values of E_a indicate that the strength of the nitrogen–oxygen bond in the N_2O molecule mainly determines the energy cost required for N_2 formation. However, in contrast to Fe-silicalite(st) possessing isolated iron species [53], the activation energy of N_2O decomposition (69 kJ mol^{-1} in Table 3) decreases over Fe-ZSM-5(st), containing also oligonuclear FeO_x species. This may be a reason for the improving effect of high-temperature steaming on the de- N_2O activity of Fe-MFI zeolites particularly below 673 K [10].

The activation energy of N_2O decomposition over *O is in the range of 81–112 kJ mol^{-1} . However, the pre-exponential factor (k^0), i.e. the collision frequency of N_2O with *O species, is strongly influenced by the type of iron species in the catalyst. These factors for Fe-silicalite(st), Fe-ZSM-5(st), and Fe-ZSM-5(lie) are 1.4×10^2 , 2.3×10^4 , and $2.9 \times 10^5 \text{ Pa}^{-1} \text{ s}^{-1}$, respectively (Table 3). The corresponding value for $\text{BaFeAl}_{11}\text{O}_{19}$ is $4.9 \times 10^2 \text{ Pa}^{-1} \text{ s}^{-1}$ and very close to that for Fe-silicalite(st). The intrinsic structure of iron species in Fe-silicalite and $\text{BaFeAl}_{11}\text{O}_{19}$ is remarkably different. Iron sites in the hexaaluminate are shielded in a crystalline framework, while isolated iron species in the zeolite are ionic species in extra-framework (ion-exchange) positions [53]. Despite these large structural differences, the degree of clustering of iron species in these both materials is very low, i.e. these species should not possess Fe–O–Fe bonds. It is important to mention that the pre-exponential factor of N_2O decomposition over *O species increases with an increase in the degree of clustering of FeO_x species on the surface of Fe-ZSM-5(st), and Fe-ZSM-5(lie). In other words, we suggest that the degree of clustering of surface and bulk FeO_x species in the zeolites and hexaaluminate, respectively, influences the collision frequency of N_2O with *O species.

An important mechanistic difference between $\text{BaFeAl}_{11}\text{O}_{19}$ and Fe-MFI relates to the pathways for O_2 formation. There are two parallel reaction pathways of O_2 formation over $\text{BaFeAl}_{11}\text{O}_{19}$: (i) N_2O

Table 3Best kinetic model and parameters of N₂O decomposition over Fe-MFI materials [23,25] derived from transient experiments in the TAP reactor^a.

| No | Elementary reaction steps | Fe-silicalite(st) | | Fe-ZSM-5(lie) | | Fe-ZSM-5(st) | |
|----|---|--------------------------|-------------------------------|--------------------------|-------------------------------|--------------------------|-------------------------------|
| | | k^0 (s ⁻¹) | E_a (kJ mol ⁻¹) | k^0 (s ⁻¹) | E_a (kJ mol ⁻¹) | k^0 (s ⁻¹) | E_a (kJ mol ⁻¹) |
| 1 | N ₂ O + * → *-O + N ₂ | 3.4 × 10 ⁵ | 120 | 4.1 × 10 ⁶ | 130 | 6.3 × 10 ² | 69 |
| 2 | N ₂ O + *-O → O-* + N ₂ | 1.4 × 10 ² | 81 | 2.9 × 10 ⁵ | 112 | 2.3 × 10 ⁴ | 98 |
| 3 | O-* → O → *-O ₂ | 9.6 × 10 ²⁰ | 300 | 2.5 × 10 ⁴ | 61 | 3.8 × 10 ¹⁰ | 142 |
| 4 | *-O ₂ → O ₂ + * | 4.4 × 10 ⁸ | 125 | 8.9 × 10 ⁸ | 58 | 2.1 × 10 ⁴ | 50 |

^a For reaction pathways 1 and 2, the pre-exponential factors are in Pa⁻¹ s⁻¹.

interacts with a surface bi-atomic oxygen species (*-O₂) yielding gas-phase O₂ and N₂ and (ii) *-O₂ can decompose to gas-phase O₂. Our micro-kinetic analysis and experimental results in Fig. 2 suggest the simultaneous formation of gas-phase O₂ and N₂ over BaFeAl₁₁O₁₉, i.e. option (i). Contrarily, the decomposition of N₂O over Fe-MFI materials is limited by the evolution of gas-phase O₂. It occurs via a complex sequence of three elementary reaction pathways: (i) N₂O reacts with an active oxygen species (*-O) yielding an adsorbed bi-atomic oxygen species (O-*O), (ii) the formed bi-atomic oxygen intermediate reorganizes into another bi-atomic one (*-O₂), and (iii) *-O₂ desorbs as O₂ generating free iron site. The micro-kinetics predicts that the degree of isolation of surface FeO_x species strongly influences the activation energy of the rearrangement of an adsorbed bi-atomic oxygen species to another one; the higher the degree of iron clustering, the easier is this rearrangement. This is probably a reason for higher de-N₂O activity of oligonuclear FeO_x species compared to isolated ones in Fe-MFI zeolites. However, the iron clustering should be optimised in order to avoid the formation of iron oxide particles, which lower the de-N₂O activity [10].

In summary, the lower de-N₂O activity of BaFeAl₁₁O₁₉ compared to Fe-MFI below 823 K can be explained as follows. According to our micro-kinetics, the overall rate of N₂O decomposition is limited by the interactions of gas-phase N₂O with iron sites possessing mono- and bi-atomic oxygen species (*-O, and *-O₂). The activity of these steps can be improved by increasing the degree of clustering of iron sites within the structure of the hexaaluminate that would imply having more iron in the hexaaluminate, i.e. by substituting more aluminum by iron in the structure. If this would be possible, Fe-hexaaluminates may approach the temperature of Fe-MFI materials in de-N₂O applications because in contrast to the latter catalysts the overall rate of N₂O decomposition over Fe-hexaaluminate is not limited by the formation of O₂.

4. Conclusions

The micro-kinetics of high-temperature direct N₂O decomposition over BaFeAl₁₁O₁₉ hexaaluminate was derived from quantitative evaluation of N₂O pulse experiments in the Temporal Analysis of Products (TAP) reactor. It was demonstrated that this approach can be successfully applied to any N₂O decomposition catalysts, covering the low and high-temperature regimes. The best kinetic model obtained via statistical discrimination of several micro-kinetic schemes consists of five elementary steps. N₂O decomposes over free iron sites as well as over iron sites with mono- and bi-atomic oxygen species originated from N₂O. The latter reaction pathway produces simultaneously gas-phase O₂ and N₂. The model was validated by its extrapolation to steady-state ambient pressure conditions and by comparison of the steady-state de-N₂O activity of BaFeAl₁₁O₁₉ with that of Fe-MFI zeolites. This also enabled us to derive mechanistic origins of distinct catalytic activity of Fe-MFI zeolites with differently clustered FeO_x species and BaFeAl₁₁O₁₉. Irrespective of the matrix for iron species, the degree of clustering of these sites appears to favor the formation of gas-phase O₂. The nature of iron species fulfils a double role:

(i) it influences the collision frequency of N₂O with iron sites in the BaFeAl₁₁O₁₉ hexaaluminate and in Fe-MFI zeolites and (ii) it decreases the activation energy of the rearrangement of adsorbed bi-atomic oxygen species in Fe-MFI.

Acknowledgement

This work was supported by the Deutsche Forschungsgemeinschaft (DFG) within the collaborative research center (Sonderforschungsbereich) 546 "Structure, dynamics and reactivity of transition metal oxide aggregates".

References

- [1] F. Kapteijn, J. Rodríguez-Mirasol, J.A. Moulijn, Appl. Catal. B 9 (1996) 25.
- [2] J. Pérez-Ramírez, F. Kapteijn, K. Schöffel, J.A. Moulijn, Appl. Catal. B 44 (2003) 117.
- [3] A. Shimizu, K. Tanaka, V. Fujimori, Chemosphere 2 (2000) 425.
- [4] J. Pérez-Ramírez, F. Kapteijn, G. Mul, J.A. Moulijn, Chem. Commun. (2001) 693.
- [5] J. Pérez-Ramírez, F. Kapteijn, G. Mul, X. Xu, J.A. Moulijn, Catal. Today 76 (2002) 55.
- [6] M. Santiago, M.A.G. Hevia, J. Pérez-Ramírez, Appl. Catal. B 90 (2009) 83.
- [7] M. Kögel, R. Monnig, W. Schwieger, A. Tissler, T. Turek, J. Catal. 182 (1999) 470.
- [8] G. Centi, L. Dall'Olio, S. Perathoner, Appl. Catal. A 194–195 (2000) 79.
- [9] K.A. Dubkov, N.S. Ovanesyan, A.A. Shteinman, E.V. Starokon, G.I. Panov, J. Catal. 207 (2002) 341.
- [10] J. Pérez-Ramírez, F. Kapteijn, J.C. Groen, A. Doménech, G. Mul, J.A. Moulijn, J. Catal. 214 (2003) 33.
- [11] L. Kiwi-Minsker, D.A. Bulushev, A. Renken, J. Catal. 219 (2003) 273.
- [12] G.D. Pirngruber, M. Luechinger, P.K. Roy, A. Cecchetto, P. Smirniotis, J. Catal. 224 (2004) 429.
- [13] E. Berrier, O. Ovsitser, E.V. Kondratenko, M. Schwidder, W. Grünert, A. Brückner, J. Catal. 249 (2007) 67.
- [14] F. Kapteijn, G. Marban, J. Rodríguez-Mirasol, J.A. Moulijn, J. Catal. 167 (1997) 256.
- [15] C.M. Fu, V.N. Korchak, W.K. Hall, J. Catal. 68 (1981) 166.
- [16] G.D. Pirngruber, J. Catal. 219 (2003) 456.
- [17] B.R. Wood, J.A. Reimer, A.T. Bell, M.T. Janicke, K.C. Ott, J. Catal. 224 (2004) 148.
- [18] E.V. Kondratenko, J. Pérez-Ramírez, Appl. Catal. A 267 (2004) 181.
- [19] A. Ates, A. Reitzmann, J. Catal. 235 (2005) 164.
- [20] A. Heyden, A.T. Bell, F.J. Keil, J. Catal. 233 (2005) 26.
- [21] A. Heyden, F.J. Keil, B. Peters, A.T. Bell, J. Phys. Chem. B 109 (2005) 1857.
- [22] N. Hansen, A. Heyden, A.T. Bell, F.J. Keil, J. Catal. 248 (2007) 213.
- [23] E.V. Kondratenko, J. Pérez-Ramírez, J. Phys. Chem. B 110 (2006) 22586.
- [24] E.V. Kondratenko, J. Pérez-Ramírez, Catal. Today 121 (2007) 197.
- [25] E.V. Kondratenko, V.A. Kondratenko, M. Santiago, J. Pérez-Ramírez, J. Catal. 256 (2008) 248.
- [26] P. Granger, P. Esteves, S. Kieger, L. Navascues, G. Leclercq, Appl. Catal. B 62 (2006) 236.
- [27] S. Alini, F. Basile, S. Blasioli, C. Rinaldi, A. Vaccari, Appl. Catal. B 70 (2007) 323.
- [28] J. Pérez-Ramírez, M. Santiago, Chem. Commun. (2007) 619.
- [29] M. Santiago, J. Pérez-Ramírez, Environ. Sci. Technol. 41 (2007) 1704.
- [30] M. Ruzak, M. Inger, S. Witkowski, M. Wilk, A. Kotarba, Z. Sojka, Catal. Lett. 128 (2008) 72.
- [31] M. Santiago, J.C. Groen, J. Pérez-Ramírez, J. Catal. 257 (2008) 152.
- [32] G. Giecko, T. Borowiecki, W. Gac, J. Kruk, Catal. Today 137 (2008) 403.
- [33] M. Tian, A. Wang, X. Wang, Y. Zhu, T. Zhang, Appl. Catal. B 92 (2009) 437.
- [34] D.V. Ivanov, E.M. Sadovskaya, L.G. Pinaeva, L.A. Isupova, J. Catal. 267 (2009) 5.
- [35] M. Santiago, M.S. Yalfani, J. Pérez-Ramírez, J. Mater. Chem. 16 (2006) 2886.
- [36] J.T. Gleaves, G.S. Yablonsky, P. Phanawadee, Y. Schuurman, Appl. Catal. A 160 (1997) 55.
- [37] J. Pérez-Ramírez, E.V. Kondratenko, Catal. Today 121 (2007) 160.
- [38] M. Rothaemel, M. Baerns, Ind. Eng. Chem. Res. 35 (1996) 1556.
- [39] M. Soick, D. Wolf, M. Baerns, Chem. Eng. Sci. 55 (2000) 2875.
- [40] R.F. Sinkovik, N.K. Madsen, ACMT. Math. Softw. 1 (1975) 232.
- [41] D. Wolf, R. Moros, Chem. Eng. Sci. 52 (1997) 1189.

- [42] W.H. Press, B.P. Flannery, S.A. Teukolsky, W.T. Vetterling, Numerical Recipes in FORTRAN, 2nd ed., Cambridge University Press, Cambridge, 1992.
- [43] G.E.P. Box, N.R. Draper, Empirical Model-Building and Response Surfaces, Wiley & Sons, New York, 1987.
- [44] D.M. Bates, D.G. Watts, Nonlinear Regression Analysis and its Application, John Wiley & Sons, New York, 1988.
- [45] K. Jířa, J. Nováková, M. Schwarze, A. Vondrová, S. Sklenák, Z. Sobalik, *J. Catal.* 15 (2009) 198.
- [46] G. Centi, A. Galli, B. Montanari, S. Perathoner, A. Vaccari, *Catal. Today* 35 (1997) 113.
- [47] J. Pérez-Ramírez, G. Mul, F. Kapteijn, J.A. Moulijn, *J. Catal.* 208 (2002) 211.
- [48] A.L. Yakovlev, G.M. Zhidomirov, R.A. van Santen, *Catal. Lett.* 75 (2001) 45.
- [49] J.A. Ryder, A.K. Chakraborty, A.T. Bell, *J. Catal.* 220 (2003) 84.
- [50] H.L. Wan, X.P. Zhou, W.Z. Weng, R.Q. Long, Z.S. Chao, W.D. Zhang, M.S. Chen, J.Z. Luo, S.Q. Zhou, *Catal. Today* 51 (1999) 161.
- [51] G. Mestl, H. Knözinger, J.H. Lunsford, Berich. Bunsen Gessel. 97 (1993) 319.
- [52] J.H. Lunsford, X. Yang, K. Haller, J. Laane, G. Mestl, H. Knözinger, *J. Phys. Chem.* 97 (1993) 13810.
- [53] J. Pérez-Ramírez, F. Kapteijn, A. Brückner, *J. Catal.* 218 (2003) 234.